EBioMedicine 2 (2015) 1500–1506

Contents lists available at ScienceDirect

EBioMedicine

journal homepage: www.ebiomedicine.com

Research Article

Grating-based X-ray Dark-field Computed Tomography of Living Mice

A. Velroyen [a,*], A. Yaroshenko [a], D. Hahn [a], A. Fehringer [a], A. Tapfer [a], M. Müller [a], P.B. Noël [b], B. Pauwels [c], A. Sasov [c], A.Ö. Yildirim [d,f], O. Eickelberg [d,f], K. Hellbach [e], S.D. Auweter [e], F.G. Meinel [e], M.F. Reiser [e,f], M. Bech [a,g], F. Pfeiffer [a,*]

[a] Lehrstuhl für Biomedizinische Physik, Physik-Department & Institut für Medizintechnik, Technische Universität München, Garching, Germany
[b] Department of Radiology, Technische Universität München, Munich, Germany
[c] Bruker microCT, Kontich, Belgium
[d] Comprehensive Pneumology Center, Institute of Lung Biology and Disease, Helmholtz Zentrum München and Ludwig-Maximilians-University Hospital Munich, Munich, Germany
[e] Institute for Clinical Radiology, Ludwig-Maximilians-University Hospital, Munich, Germany
[f] German Center for Lung Research (DZL), Germany
[g] Medical Radiation Physics, Lund University, Lund, Sweden

ARTICLE INFO

Article history:
Received 11 June 2015
Received in revised form 4 August 2015
Accepted 5 August 2015
Available online 13 August 2015

Keywords:
Dark-field imaging
Dark-field computed tomography
Pulmonary emphysema
Pulmonary fibrosis
X-ray phase-contrast imaging

ABSTRACT

Changes in x-ray attenuating tissue caused by lung disorders like emphysema or fibrosis are subtle and thus only resolved by high-resolution computed tomography (CT). The structural reorganization, however, is of strong influence for lung function. Dark-field CT (DFCT), based on small-angle scattering of x-rays, reveals such structural changes even at resolutions coarser than the pulmonary network and thus provides access to their anatomical distribution. In this proof-of-concept study we present x-ray *in vivo* DFCTs of lungs of a healthy, an emphysematous and a fibrotic mouse. The tomographies show excellent depiction of the distribution of structural – and thus indirectly functional – changes in lung parenchyma, on single-modality slices in dark field as well as on multimodal fusion images. Therefore, we anticipate numerous applications of DFCT in diagnostic lung imaging. We introduce a scatter-based Hounsfield Unit (sHU) scale to facilitate comparability of scans. In this newly defined sHU scale, the pathophysiological changes by emphysema and fibrosis cause a shift towards lower numbers, compared to healthy lung tissue.

1. Introduction

Lung diseases pose one of the leading causes of death worldwide (World Health Organization, 2011). A large fraction of those mortality numbers is represented by chronic obstructive pulmonary disease (Zvezdin et al., 2009), of which lung emphysema is a common component. The disease is associated with inflammatory processes in lung tissue caused most commonly by smoking. In consequence, the alveolar walls necessary for gas exchange in the blood are destroyed, resulting in enlarged distal air spaces and consequently deteriorated lung function and decreased quality of life (Ley-Zaporozhan et al., 2008). Pulmonary fibrosis can be idiopathic or caused by inhalation of pollutants, infection, or adverse reactions to drugs (Bourke, 2006). In the course of this interstitial lung disease normal parenchyma is gradually replaced by connective tissue (scarring), resulting in a restricted lung and impaired gas exchange (King, 2005). The sensitivity and specificity of conventional x-ray projection radiography in diagnosing those disorders is low for mild to moderate stages (King, 2005; Washko, 2010), and lung function testing is still gold standard, while direct assessment of the microstructural changes and disease progression is only available *via* invasive biopsy. Attenuation-based high-resolution computed tomography (HRCT) serves for improved emphysema and fibrosis imaging, also providing information about the three-dimensional regional distribution of the disease necessary for lung volume reduction surgery (Washko et al., 2008; Criner and Mamary, 2010), but its use is limited due to the required substantial radiation dose (Washko, 2010).

Contrary to conventional medical x-ray imaging, grating-based phase-contrast and dark-field imaging (PCI/DFI) generate contrast from perturbations in the x-ray wave-front caused by refraction and ultra-small angle scattering in tissue (Weitkamp et al., 2005). Its proven feasibility with conventional polychromatic x-ray sources (Pfeiffer et al., 2008; Pfeiffer et al., 2006) has recently triggered developments towards preclinical and clinical translation, such as *in vivo* radiographic projection imaging (Bech et al., 2013) at a dedicated preclinical table-top scanner (Tapfer et al., 2012). Earlier *in vivo* studies using different PCI/DFI techniques were restricted to synchrotron radiation or very small field of view (Bravin et al., 2013). However, the benefit of exploiting

* Corresponding authors.
E-mail addresses: astrid.velroyen@ph.tum.de (A. Velroyen), franz.pfeiffer@tum.de (F. Pfeiffer).

http://dx.doi.org/10.1016/j.ebiom.2015.08.014

refractive index differences in x-ray imaging of weakly absorbing airways tissue could already be demonstrated *in vivo* at the synchrotron (Lewis et al., 2005). In preceding studies, we introduced emphysema diagnosis on living mice based on x-ray scatter-based dark-field projection imaging (Meinel et al., 2014; Hellbach et al., 2015).

In this work, we present the first successful x-ray dark-field (DF) computed tomography (CT) scans of *in vivo* mice with a dedicated micro-CT scanner (Tapfer et al., 2012). To exploit the DF signal's ability to depict sub-resolution microstructures, thoracic tomographies were acquired of a healthy control mouse, a mouse with pulmonary emphysema and a mouse with pulmonary fibrosis. The scope of this study is to highlight the feasibility and demonstrate the potential diagnostic benefit of the novel contrast modality in three-dimensional imaging. Complementary to the quantitative Hounsfield scale in attenuation-based CT, we also introduce a scatter-based Hounsfield scale for quantitative DFCT of lung tissue.

2. Materials & Methods

2.1. Murine Model

Animals were housed in SPF rooms maintained at constant temperature and humidity with a 12-h light cycle and were allowed food and water *ad libitum*. All experiments were conducted under strict governmental (GV-SOLAS) and international guidelines (FELASA) and were approved under number 2532-77-12 by the local government for the administrative region of Upper Bavaria. For this study 6 to 8 week old pathogen-free female C57BL/6N (Charles River Laboratories, Sulzfeld, Germany) mice were used. Pulmonary emphysema was introduced by orotracheal application of an 80 µl solution of porcine pancreatic elastase (80 U per kilogram bodyweight; Sigma-Aldrich, Munich, Germany) in sterile phosphate-buffered saline (PBS). Pulmonary fibrosis was provoked by orotracheal insertion of 2.5 U bleomycin per kg bodyweight. The control animal was treated with 80 µl PBS only. Treatments were performed under anesthesia by intraperitoneal injection of medetomidine (500 µg/kg), midazolam (5 mg/kg) and fentanyl (50 µg/kg). The anesthesia was then antagonized with a subcutaneous injection of atipamezole (50 mg/ml), fulimazenil (0,1 mg/ml) and naloxone (0,4 mg/ml). Control and emphysema mouse were scanned 21 days, fibrosis mouse 14 days after application.

2.2. Grating-based Dark-field and Phase-contrast Imaging

To measure perturbations of the x-ray wave front other than the mere attenuation and to subsequently extract the dark-field and phase-contrast signals, it is necessary to place optical elements, in our case grating structures, into the x-ray beam path between source and detector. The three gratings as displayed in the sketch in Fig. 1 a comprise the so-called Talbot–Lau interferometer: The source grating G0 counteracts the incoherence of the extended and polychromatic conventional x-ray source by creating an array of smaller line sources that exhibit sufficient coherence. The phase grating G1 acts as a beam splitter generating an interference pattern downstream. Relative to an empty beam, placing an object into the setup influences the interference pattern in three different ways: First, the overall intensity drops due to *attenuation*. Second, the pattern is laterally shifted if the x-rays undergo a resolvable refraction in the material, which is exploited as the (differential) *phase contrast* (for the sake of simplicity not shown in the sketch). Third, scattering of the x-rays at microstructures that cannot be spatially resolved by the imaging system causes the minima and maxima of the interference pattern to be less pronounced, which is translated into the *dark-field* signal. As the pattern cannot be resolved directly by the detector pixel size, the analyzer grating G2 is used to sample the intensity variation: In a process called 'phase stepping' (Weitkamp et al., 2005), several images are acquired at different lateral positions of the three gratings relative to one another over one period of the pattern. The intensity thereby recorded in one detector pixel over the grating position can be described by a sinusoidal curve that changes its parameters offset, phase, and amplitude between an empty beam (reference) and an object in the beam (see Fig. 1 b). Using sinusoidal fits or Fourier analysis, attenuation, differential phase and dark-field signal are extracted respectively from the parameters of the two curves. Thus three different modalities per projection angle are acquired. As in conventional CT, a three dimensional representation of the object can be calculated also for dark-field and phase-contrast imaging, using tomographic image reconstruction algorithms.

2.3. Scanner Setup

The images were acquired using a dedicated small-animal x-ray dark-field and phase-contrast CT scanner developed in collaboration with *Bruker microCT* (Tapfer et al., 2012). The scanner comprises a setup consisting of detector (flatpanel by Hamamatsu C9312SK-6), source (tungsten-target x-ray tube RTW, MCBM 65B-50 W, approx. 50 µm focal spot) and Talbot–Lau interferometer on a rotating gantry and facilities to monitor heart beat, breathing motion and temperature of the animal. The gratings of the interferometer are specified by the following bar materials, heights, and periods, respectively: G0 — gold, 35 µm, 10 µm; G1 — nickel, 4 µm, 3.2 µm; G2 — gold 45 µm, 4.8 µm.

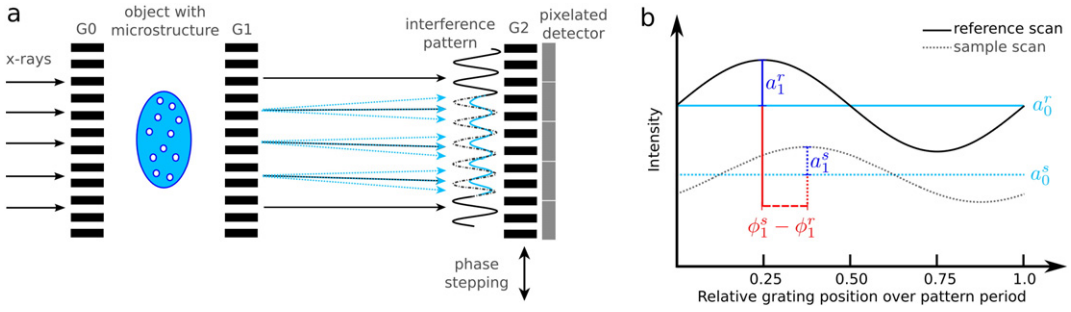

Fig. 1. Methodology of grating-based dark-field and phase-contrast imaging. **a**: Sketch of a Talbot–Lau interferometry setup. By the use of three optical grating structures (source grating G0, phase grating G1, analyzer grating G2) the perturbations introduced by the sample to the x-ray wave front are translated into intensity variations that can be measured by the x-ray detector. The original (reference) interference pattern created by G1 (dashed and solid black line) is changed by the presence of the object in terms of overall intensity (decreased offset of blue line) due to attenuation, and in terms of smoothing of the extrema (reduced peaks and valleys of the blue line) due to scattering at microstructures. Resolvable refraction of the x-rays in the sample would result in a lateral shift of the blue relative to the black dashed line (not shown here for the sake of simplicity). By recording images with the detector at different grating positions over one period of the interference pattern ('phase stepping'), the pattern is sampled. **b**: Measured intensity in one detector pixel for a reference (empty beam, superscript r) and a sample scan (superscript s) over one phase-stepping cycle. By determining the change of the parameters offset a_0, amplitude a_1, and relative phase ϕ_1, the three signals attenuation, dark-field, and phase are extracted.

2.4. Acquisition

The mice were anesthetized as during emphysema or fibrosis introduction (see *Murine model*) and placed on the sample bed in supine position. During acquisition they were breathing freely. Body temperature and respiratory movement were constantly monitored and the temperature was kept stable *via* a built-in warm-air fan. All scans were acquired at a source voltage of 35 kVp and a current of 524 μA. The detector was operated in 2-by-2 binning mode, resulting in an effective pixel size of 58 μm. According to the phase stepping method (Weitkamp et al., 2005), for each angular gantry position a set of five images with varying source-grating position was recorded applying an exposure of 5 s. For each animal 139 angular views distributed over 360° were taken, resulting in a total exposure time of approximately one hour and an accumulated dose of 200 mGy. For processing of the raw phase stepping data, reference sets of phase steps were acquired each time when the scan had progressed ten angular gantry positions. For this, the mice were temporarily moved out of the beam path.

2.5. Raw Data Processing

Prior to extraction of attenuation, differential phase and dark-field signal, the raw stepping images were sharpened using Richardson–Lucy deconvolution with the measured point-spread function of the imaging system. Since the three modalities have differing noise behaviors, the number of deconvolution iterations was optimized for each imaging channel individually, resulting in zero iterations for dark field, one iteration for attenuation and three iterations for differential phase images. To extract attenuation, differential phase and dark-field signal from the phase stepping sets a pixel-wise sine fit function was applied, which additionally provides the variances on the signals that are required for the applied reconstruction technique. To counteract distortions in the phase image caused by thermal and mechanical influences on the grating structures, an adaptive phase recovery tool was applied as described by Tapfer et al. (2012), but with the extension of using a surface fit, described by a polynomial of degree 2, to the sample-free image margin instead of a ramp fit over the complete image. Transmission and dark-field images were corrected for variations in intensity by a simple background normalization using areas with no sample coverage. Since all three imaging channels are extracted from the same raw stepping set, the modalities are inherently perfectly co-registered.

2.6. Tomographic Reconstruction

As the mice cover approximately 675 pixels in width of the field of view, the scans are severely undersampled due to time constraints posed by the anesthesia duration. To partly cope with the resulting artifacts in the tomographic reconstruction, a statistical iterative reconstruction technique, described in detail by Hahn et al. (Hahn et al., 2015), was applied with parameters optimized for each modality individually but consistent between the datasets of the three mice. To counteract overregularization and loss of detail in case of the attenuation CT, the noise power spectrum of the three mice datasets were adjusted by weighting iterative reconstruction and conventional filtered back-projection reconstruction (with Ram-Lak filter) with 0.75 and 0.25 respectively.

2.7. Post-processing

For representation and analysis purposes simple semi-automated threshold-based segmentation was applied to differentiate mouse torso, skeleton, lung, and surrounding air and animal bed by use of the commercially available Software VGStudioMax 2.0 (Volume Graphics, Heidelberg, Germany). In doing so, only minor manual corrections were necessary. The segmentation of the mouse torso from surrounding structures was performed on the phase-contrast dataset, because it contained the fewest artifacts influencing the outer shape of the mouse. Segmentation of the bones and the lungs was performed based on the attenuation data and the dark-field data respectively, exploiting their modality-inherent strongest signal differences to the surrounding tissue. The perfect co-registration allows for simple transfer of a segmentation in one modality to the volumes of the other modalities. The volume and surface renderings for the three-dimensional representations (Fig. 3) and the supplemental movie (S2) of the datasets were performed by Volume Graphics based on the aforementioned segmentations. The fusion images shown in Fig. 2 were created from the isolated torsos in attenuation (gray) and dark field (hot color scheme) using the image fusion tool of OsiriX Imaging Software v.3.7.1 64-bit (by Antoine Rosset) with the setting of 50% fusion and a manual windowing for best visual appearance.

2.8. Histogram Analysis

To obtain a voxel set that objectively fully contains the lung for comparison of the dark-field CT gray-value distributions between the mice, the threshold-based segmentations (optimized for visual appearance) were strongly dilated, so that a volume that comprises lung and partly surrounding non-scattering soft tissue was achieved. Since apart from lung tissue only the granular structure of bones can be a possible source of scattering in this region, the rib cage was subtracted from this volume. The histograms shown in Fig. 4 represent the gray-value distribution of the remaining volumes. Since the processing, tomographic reconstruction and post-processing was equivalent for each mouse dataset, the distributions can be assumed quantitatively comparable among each other. A peak-finder function was applied to a multi-Gauss fit of the histogram curves to determine the positions of the zero-scatter peaks of all three mice and the lung peaks of control and emphysematous mouse without influence of local extrema. The rescaling of gray values (tiff range) to scatter Hounsfield Units (HUs) was done by setting the mean of the three zero-scatter peak positions to 0 HUs and the location of lung peak of the control mouse to 1000 HUs.

2.9. Histology

After excision, the lungs were fixated in paraformaldehyde for conservation during transport. They were subsequently washed to remove the formalin solution and then decalcified in a 10% EDTA solution for 5 days. The samples were dehydrated and embedded in paraffin. In the coronal plane, multiple 10 μm thin slices were prepared at an interval of 0.5 mm. After deparaffinization and hydration the slices were stained using Mayer's hematoxylin and eosin (HE). Ultimately, they were dehydrated and scanned.

3. Results

Fig. 2 provides an overview over the CT datasets of this study comprising three *in vivo* cases imaged in conventional attenuation and DF, as well as correspondent histological slices to illustrate the nature of the respective disease. Additionally, phase-contrast CT slices are presented in supplemental Fig. S1. Comparing the conventional CT scan of the emphysematous mouse (Fig. 2 b, e) with the control (Fig. 2 a, d), one observes only subtle differences towards darker gray values in peripheral lung tissue in the emphysematous case. The resolution of the imaging system does not allow a direct depiction of the alveolar wall structure. In the respective CT slices of the DF channel (Fig. 2 g, j for control, h, k for emphysema) the strong difference in signal allows for clear discernibility between control and diseased case, as visible by the overall reduced brightness and decreased homogeneity in the diseased lung compared to the healthy lung. The destruction of alveolar walls and resulting enlargement of air spaces (as displayed in the corresponding histological section in Fig. 2 n) causes significantly reduced x-ray

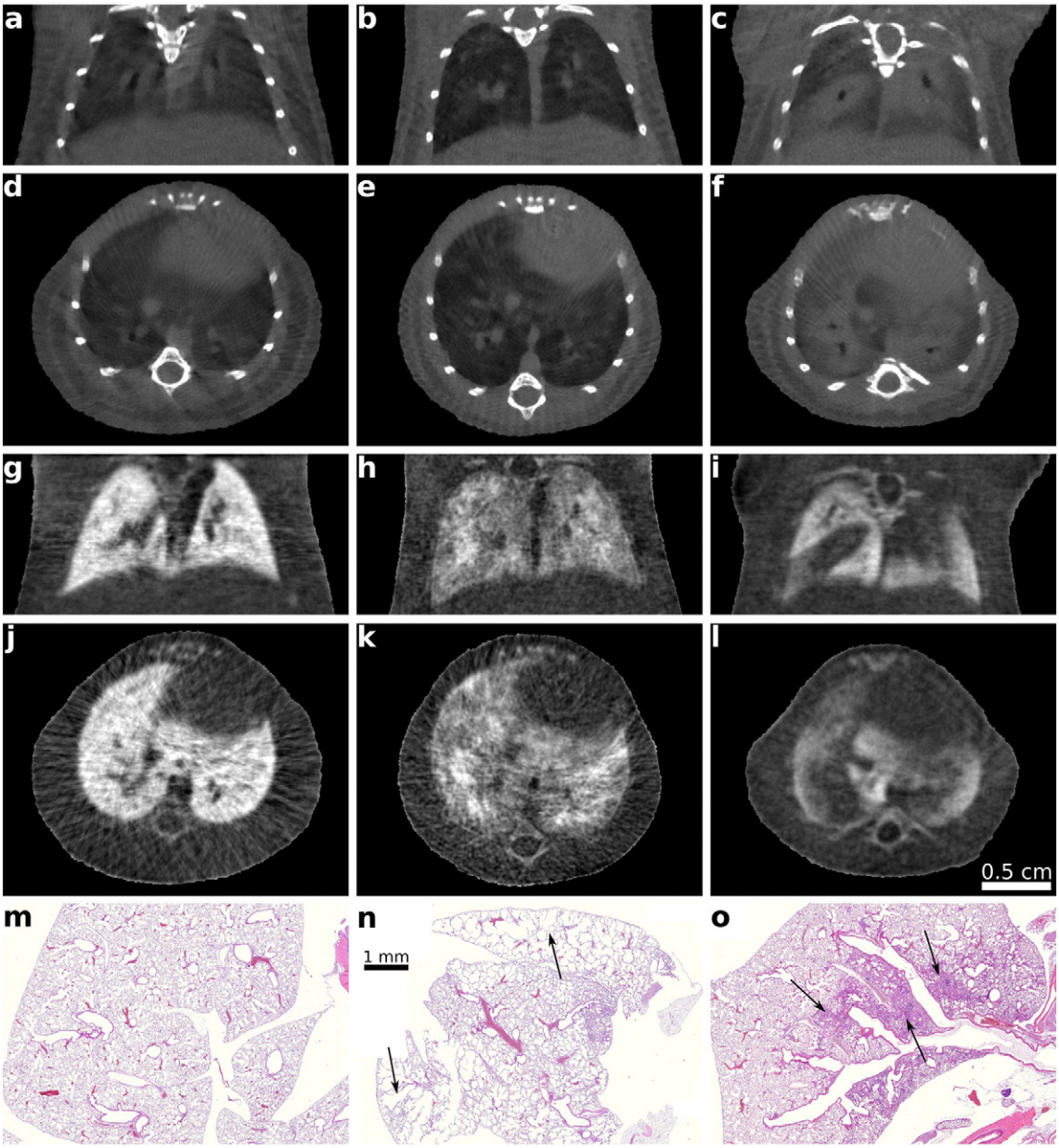

Fig. 2. Exemplary attenuation and dark-field CT slices and histological sections of lungs of three *in vivo* mice. Pathophysiological changes are subtle in the attenuation-based, but clear in scatter-based CT images as visible by the overall reduced brightness and decreased homogeneity of the signal in the diseased lungs compared to the healthy lung. Gray-value windows chosen for best visual appearance, but consistent within the same modality, respectively. Left-most column: Control mouse. Center column: Emphysematous mouse. Right-most column: Fibrotic mouse. **a–c**: Coronal slices of attenuation CT. **d–f**: Axial slices of attenuation CT. **g–i**: Coronal slices of dark-field CT. **j–l**: Axial slices of dark-field CT. **m–o**: Histopathological slices (HE-stained) of the lungs.

scattering, while the overall loss of tissue and the resulting attenuation decrease is weak.

When concentrating on the case of lung fibrosis (Fig. 2 c, f for attenuation, i, l for DF) the replacement of functional alveolar network by solid scar tissue is clearly apparent in both modalities, since the presented case is at an advanced stage. The DF image reveals areas with remaining functional alveolar structure. Histology illustrates the scarring in the lung (Fig. 2 o), compared to healthy lung tissue (Fig. 2 m).

Fig. 3 shows a volumetric overview of the fusion of the attenuation CT and DFCT for the two pathological cases emphysema (a–f) and fibrosis (g–l). The fused representation, which is easily possible due to the method-inherent perfect co-registration, provides a simultaneous impression of anatomy depicted by the attenuation CT and functionality indirectly displayed by DFCT, since alveolar structure can be related to quality of gas exchange (Haraguchi et al., 1998). Similar to the function-anatomy combination in well-known multi-modal datasets like PET–CT (PET: positron emission tomography), the conventional attenuation CT images in gray shades were overlaid by DF data in PET-typical hot color scheme. Note, however, that contrary to PET, where hot areas indicate accumulation of tracer and therefore generally diseased tissue, in the displayed fusion images the brighter color codes the stronger scattering, *i.e.* the more intact or healthier lung tissue. The combined representation allows for a comprehensive depiction of the three-dimensional distribution of the diseases over the lung volume in the anatomical frame. In the case of emphysema Fig. 3 shows that destruction of alveolar structures and size increase of air voids predominantly appears in peripheral regions of the lung as indicated by white arrows. On the contrary, in Fig. 3 g–l arrows illustrate that the proliferation of the induced fibrosis concentrates on the central, peribronchial areas. Regarding the inherent complementarity of the two signals,

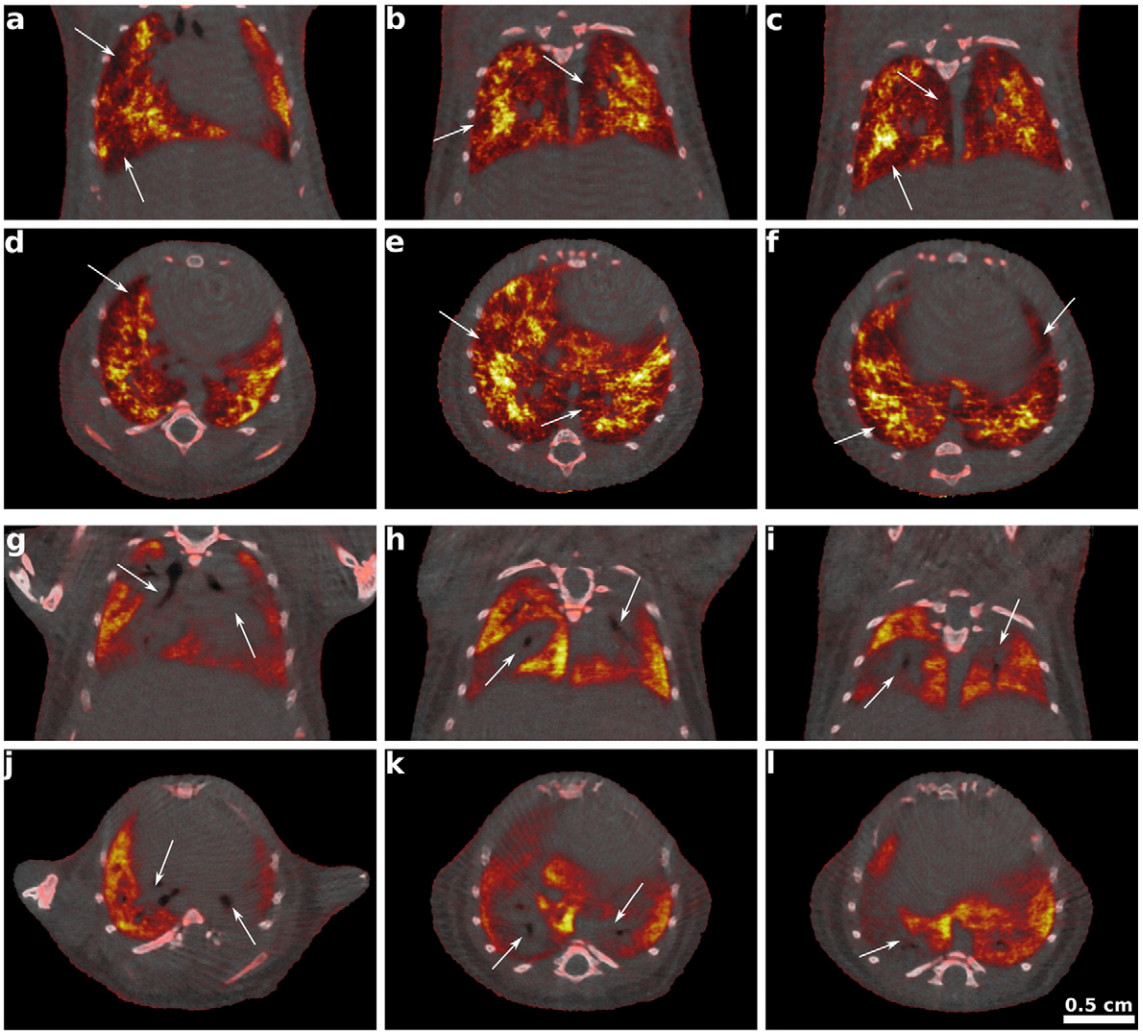

Fig. 3. Fusion images of attenuation and dark-field CT of mouse with emphysematous lung (**a–f**) and mouse with fibrotic lung (**g–l**) at different positions in the three-dimensional volume. Emphysema case: Dark red areas indicating regions with strongly reduced scattering abilities (but little absorption) appear preferentially in the peripherals of the lung (white arrows). **a–c**: Anterior to posterior coronal slices. **d–f**: Cranial to caudal axial slices. Fibrosis case: Red areas exhibit reduced scattering ability than bright yellow regions and match here with excessive tissue marked by enhanced absorption in attenuation CT. Arrows indicate the preferential spreading of the scarring along the bronchi. **g–i**: Anterior to posterior coronal slices. **j–l**: Cranial to caudal axial slices.

note that in DF large air-filled voids such as the bronchi are coded identically to solid soft tissue, whereas they are distinguishable in attenuation data.

The complementarity of the DF signal with regard to the conventional attenuation-based signal allows for excellent differential diagnosis between the two disorders emphysema and fibrosis. While both typical structural changes caused by the two disorders result in reduced scattering of x-rays and thus decreased dark-field signal, the combination with the always inherently co-registered attenuation signal allows for a distinction about the type of structural change, as the fibrotic parenchyma usually exhibits a stronger attenuation.

For a better three-dimensional impression Fig. 4 provides exemplary views of volume renderings of the acquired datasets. Bones were segmented from the attenuation signal, whereas lung tissue was extracted from the DFCTs and represented by a semi-transparent hot color map to enhance inter- and intra-pulmonary structural variations. The 3D views confirm the earlier findings from the 2D slices: The control lung exhibits a strong homogeneous scattering pattern all over its volume, whereas the emphysema lung shows reduced scattering in the periphery and the fibrotic lung lacks scattering areas in the central, peribronchial regions. In the supplemental material, we provide an animation of the rendered multi-modal volumes (see Movie S2) to allow for a three-dimensional assessment from different viewing angles.

The strong difference in the identically windowed scatter-based gray-values between the cases (Fig. 2 g–l) suggests that differentiation between diseased and healthy tissue merely based on DF signal strength is possible. For a closer analysis, the histograms of the three lung-tissue volumes (including a non-scattering soft-tissue margin) are shown in Fig. 5. In attenuation-based CT – and recently in phase-contrast CT (Donath et al., 2010) – , universal Hounsfield Units (HU) were established to facilitate comparability of data acquired at different scanners. As an analogue approach, we introduce scatter-based Hounsfield Units (HUs). The established HU scales are defined *via* their tomographically reconstructed signals for water (0 HU) and for air (−1000 HU), such that the HU number for tissue x is calculated *via* the linear attenuation coefficient μ_x in case of the attenuation HU scale:

$$\mathrm{HU}_x = 1000 \cdot \frac{\mu_x - \mu_{water}}{\mu_{water} - \mu_{air}}.$$

However, this definition cannot be transferred to DFCT, since both water and air do not scatter and thus produce identical signals. Therefore, we suggest the usage of a zero-scatter reference area to determine 0 HUs. This can be either water or air, or – in our case – non-scattering solid soft-tissue, as it is included in the histogram-analyzed volume for each of the three cases. The non-scattering parts form the three

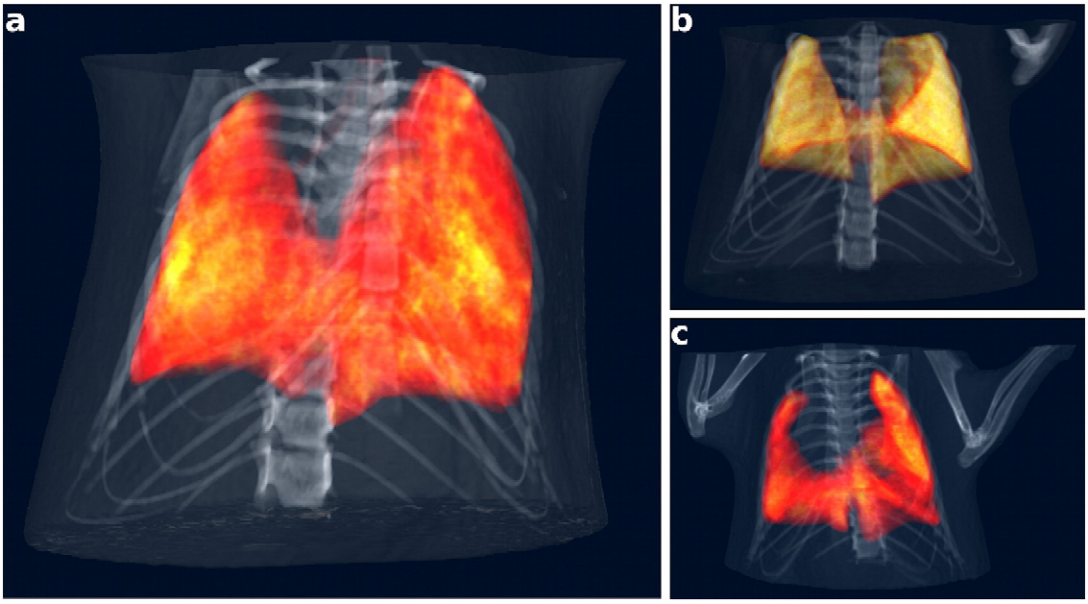

Fig. 4. Volume renderings of **a**: emphysematous, **b**: control and **c**: fibrotic case. The skeletal structure was segmented from attenuation CT, whereas the lung tissue was extracted from dark-field CT and represented by a semi-transparent hot color map. The renderings show the volumetric distribution of the overall reduced signal and its decreased homogeneity in the diseased lungs compared to the healthy lung.

overlapping peaks to the left of the histogram range. To span a range of 1000 HUs we propose the peak position of the strongest scatterer in our measurements, the control lung, as reference point for 1000 HUs. Using the linear diffusion coefficient ε_x as a measure for the scattering strength of a material x as suggested by Bech et al. (Bech et al., 2010), we obtain the definition

$$\mathrm{HUs}_x = 1000 \cdot \frac{\varepsilon_x - \varepsilon_0}{\varepsilon_{\mathrm{Control}} - \varepsilon_0},$$

where ε_0 is the linear diffusion coefficient of a non-scattering area, so ideally equal to 0, and $\varepsilon_{\mathrm{Control}}$ describes healthy lung tissue.

Hereby, destruction of alveolar structures results in a shift of the main pulmonary peak towards the zero-scatter point, as it is the case for the emphysematous lung with a peak position at approximately 373 HUs. Elimination of the air-filled voids is so advanced in some areas of the fibrotic lung, that the pulmonary peak merges into the zero-scatter peak in this case. The increased peak height of the zero-scatter peak reflects the substitution of those voids by non-scattering solid soft tissue.

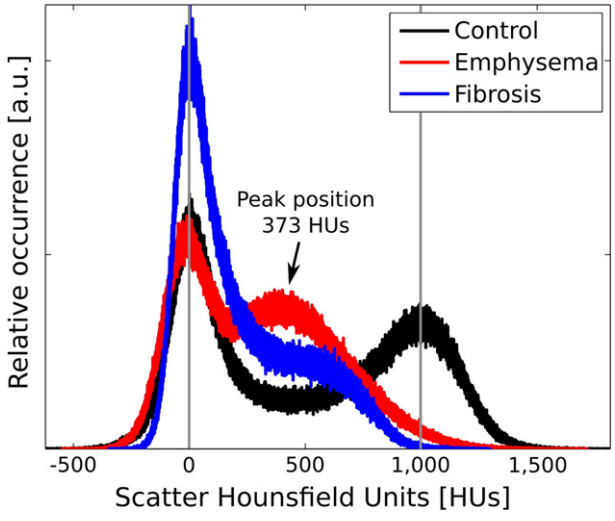

Fig. 5. Histograms of the scatter-based gray values of the extended lung region of dark-field CT volumes of control (black), emphysematous (red) and fibrotic (blue) mouse. The gray values are scaled according to the novel scatter Hounsfield Units (HUs) introduced in the text. The pathophysiological changes of emphysematous and fibrotic lung cause a shift towards lower HUs. Peaks at 0 HUs correspond to non-scattering solid soft-tissue areas surrounding the actual alveolar lung region.

4. Discussion

The presented results reflect a proof-of-principle demonstration of *in vivo* DFCT imaging and its possible benefits in non-invasively evaluating pulmonary pathophysiology. For a detailed analysis of sensitivity and specificity for diagnosing various lung diseases, studies with larger sample sizes and several disease stages are required. To this end, our results show that this is in general feasible as dose-compatibility for longitudinal studies on small animals is given. Moreover, a whole atlas of healthy lung measurements should be developed to serve for sound establishment of the suggested lung-specific HUs reference point, and is beyond the scope of this proof-of-principle study. Ultimately, a standardized lung phantom needs to be developed based on this atlas to guarantee reliable comparability of the HUs scale from different scanners, because the DF signal strength depends on various parameters such as feature (alveolar) size, x-ray energy or interferometer specifications. We also want to point out that the applicability of a lung-based HUs scale to other DFI applications, for example bones (Potdevin et al., 2012), remains to be verified, since alternate applications may demand setups of higher sensitivity.

To reach clinical application cases, certain technological limitations of the method need to be overcome, but are already subject to currently on-going research and development efforts: For example, when translating the method to an increased torso diameter, an elevated x-ray energy is mandatory to reach the necessary penetration depth. The main technological challenge is the manufacturing of high-aspect-ratio grating structures suitable for clinical energies, covering a large field of view (FOV). While sufficiently high aspect ratios have been demonstrated in experiment already (Willner et al., 2013; Ruiz-Yaniz et al., 2015; Sarapata et al., 2014), the increase of the FOV by tiling gratings together (Meiser et al., 2014) is under development. Concerning the dark-field signal strength, simulations and yet unpublished experiments have indicated the feasibility of x-ray dark-field projection imaging at clinically

relevant x-ray energies on thick samples. Furthermore, to reduce dose and scan time for clinical compatibility, acquisition schemes alternative to the established 'phase stepping' (Weitkamp et al., 2005) have been proposed (Zanette et al., 2011, 2012) and are being further investigated.

Despite the limited sample size of three cases in the present study, the presented results prove great potential for future lung imaging where volumetric information such as disease distribution is required. One example is the use of x-ray scatter CT for the evaluation of potential lung volume reduction surgery candidates (Washko, 2010) in case of emphysema. In general, mild stages of emphysema are difficult to diagnose by projection radiography only and often dose-intensive HRCT is needed. Projection-based DFI may ultimately serve as a screening method (Hellbach et al., 2015; Meinel et al., 2014; Schleede et al., 2012; Yaroshenko et al., 2013). We imagine to complement this by limited-angle or coarse-resolution DFCT to gain additional three-dimensional information without the necessity of very high dose, exploiting that DFI generates a signal from structure sizes below the resolution limit of the imaging system (Chen et al., 2010; Yashiro et al., 2010; Lynch et al., 2011). The presented CT results already serve as an example for non-optimized resolution settings, because they are subject to undersampling and breathing-motion artifacts due to non-gated acquisition and long exposure times. This is possible as DFI profits more from noise reduction when changing to coarser resolution and suffers less from the loss of detail than conventional attenuation (Velroyen et al., 2013). Another conceivable application of thoracic DFCT is to map suspicious pulmonary parenchyma in case of suspected fibrosis, without the need to force the spatial resolution down to the level of the secondary pulmonary lobule. This may allow optimization of the location choice for biopsy, which is still the gold standard for diagnosing idiopathic interstitial pneumonias and currently done with the help of attenuation-based HRCT (Gross and Hunninghake, 2001).

Supplementary data to this article can be found online at http://dx.doi.org/10.1016/j.ebiom.2015.08.014.

Author Contributions

A. Ö. Y., O. E., F. G. M., M. F. R., S. D. A., M. B. and F.P. designed the study. A. T., B. P., A. S., A. Y., M. B., A. V. and F. P. lay indispensable technological ground work for the study in developing the small-animal DFCT scanner. A. Y., M. M. and K. H. performed the scans. A. V., D. H., A. F., P. B. N., K. H., M. B. and F.P. conducted data processing, reconstruction and analysis. A. V., A. Y., B. P., A. S., A. Ö. Y., O. E., K. H., F. G. M., M. B. and F. P. wrote the paper. All authors reviewed the manuscript.

Conflict-of-interest Statement

B. P. and A. S. are employees of Bruker microCT. All other authors declare no conflict of interest.

Acknowledgments

We acknowledge the help of C. Hollauer and J. Hostens for the productive support with the experiments. We acknowledge financial support through the DFG Cluster of Excellence Munich-Centre for Advanced Photonics (MAP, Grant no. DFG EXC-158), the DFG Gottfried Wilhelm Leibniz program and the European Research Council (ERC, FP7, StG 240142). This work was carried out with the support of the Karlsruhe Nano Micro Facility (KNMF, www.kit.edu/knmf), a Helmholtz Research Infrastructure at Karlsruhe Institute of Technology (KIT, www.kit.edu). The funders had no role in study design, data collection, data analysis, interpretation, or writing of the report. AV and AY acknowledge the TUM Graduate School. The graphical rendering (3D figures and movie) was performed by Volume Graphics, Heidelberg, Germany.

References

Bech, M., Bunk, O., Donath, T., et al., 2010. Quantitative x-ray dark-field computed tomography. Phys. Med. Biol. 55, 5529–5539.
Bech, M., Tapfer, A., Velroyen, A., et al., 2013. In-vivo dark-field and phase-contrast x-ray imaging. Sci. Rep. 3, 3209. http://dx.doi.org/10.1038/srep03209.
Bourke, S.J., 2006. Interstitial lung disease: progress and problems. Postgrad. Med. J. 82, 494–499.
Bravin, A., Coan, P., Suortti, P., 2013. X-ray phase-contrast imaging: from pre-clinical applications towards clinics. Phys. Med. Biol. 58, R1–R35.
Chen, G.-H., Bevins, N., Zambelli, J., Qi, Z., 2010. Small-angle scattering computed tomography (SAS-CT) using a Talbot–Lau interferometer and a rotating anode x-ray tube: theory and experiments. Opt. Express 18, 12960–12970. http://dx.doi.org/10.1364/OE.18.012960.
Criner, G.J., Mamary, A.J., 2010. Lung volume reduction surgery and lung volume reduction in advanced emphysema: who and why? Semin. Respir. Crit. Care Med. 31, 348–364.
Donath, T., Pfeiffer, F., Bunk, O., et al., 2010. Toward clinical x-ray phase-contrast CT: demonstration of enhanced soft-tissue contrast in human specimen. Invest. Radiol. 45, 445–452.
Gross, T., Hunninghake, G., 2001. Idiopathic pulmonary fibrosis. N. Engl. J. Med. 345, 517–525.
Hahn, D., Thibault, P., Fehringer, A., et al., 2015. Statistical iterative reconstruction algorithm for X-ray phase-contrast CT. Sci. Rep. 5, 10452.
Haraguchi, M., Shimura, S., Hida, W., Shirato, K., 1998. Pulmonary function and regional distribution of emphysema as determined by high-resolution computed tomography. Respir. Int. Rev. Thorac. Dis. 65, 125–129.
Hellbach, K., Yaroshenko, A., Meinel, F.G., et al., 2015. In vivo dark-field radiography for early diagnosis and staging of pulmonary emphysema. Investig. Radiol. 50, 430–435.
King, T.E., 2005. Clinical advances in the diagnosis and therapy of the interstitial lung diseases. Am. J. Respir. Crit. Care Med. 172, 268–279.
Lewis, R.A., Yagi, N., Kitchen, M.J., et al., 2005. Dynamic imaging of the lungs using x-ray phase contrast. Phys. Med. Biol. 50, 5031–5040.
Ley-Zaporozhan, J., Ley, S., Kauczor, H.U., 2008. Morphological and functional imaging in COPD with CT and MRI: present and future. Eur. Radiol. 18, 510–521.
Lynch, S.K., Pai, V., Auxier, J., et al., 2011. Interpretation of dark-field contrast and particle-size selectivity in grating interferometers. Appl. Opt. 50, 4310–4319.
Meinel, F.G., Yaroshenko, A., Hellbach, K., et al., 2014. Improved diagnosis of pulmonary emphysema using in vivo dark-field radiography. Invest. Radiol. 49, 653–658.
Meiser, J., Amberger, M., Willner, M., et al., 2014. Increasing the field of view of x-ray phase contrast imaging using stitched gratings on low absorbent carriers. Proc. SPIE Med. Imaging 903355.
Pfeiffer, F., Weitkamp, T., Bunk, O., David, C., 2006. Phase retrieval and differential phase-contrast imaging with low-brilliance x-ray sources. Nature Phys. 2, 258–261.
Pfeiffer, F., Bech, M., Bunk, O., et al., 2008. Hard-x-ray dark-field imaging using a grating interferometer. Nat. Mater. 7, 134–137.
Potdevin, G., Malecki, A., Biernath, T., et al., 2012. X-ray vector radiography for bone micro-architecture diagnostics. Phys. Med. Biol. 57, 3451–3461.
Ruiz-Yaniz, M., Koch, F., Zanette, I., et al., 2015. X-ray grating interferometry at photon energies over 180 keV. Appl. Phys. Lett. 106, 151105.
Sarapata, A., Stayman, J.W., Finkenthal, M., et al., 2014. High energy x-ray phase contrast CT using glancing-angle grating interferometers. Med. Phys. 41, 021904.
Schleede, S., Meinel, F.G., Bech, M., et al., 2012. Emphysema diagnosis using x-ray dark-field imaging at a laser-driven compact synchrotron light source. Proc. Natl. Acad. Sci. U. S. A. 109, 17880–17885.
Tapfer, A., Bech, M., Velroyen, A., et al., 2012. Experimental results from a preclinical x-ray phase-contrast CT scanner. Proc. Natl. Acad. Sci. U. S. A. 109, 15691–15696.
Velroyen, A., Bech, M., Malecki, A., et al., 2013. Microbubbles as a scattering contrast agent for grating-based x-ray dark-field imaging. Phys. Med. Biol. 58, N37–N46.
Washko, G.R., 2010. Diagnostic imaging in COPD. Semin. Respir. Crit. Care Med. 31, 276–285.
Washko, G.R., Hoffman, E., Reilly, J.J., 2008. Radiographic evaluation of the potential lung volume reduction surgery candidate. Proc. Am. Thorac. Soc. 5, 421–426.
Weitkamp, T., Diaz, A., David, C., et al., 2005. X-ray phase imaging with a grating interferometer. Opt. Express 13, 6296–6304. http://dx.doi.org/10.1364/OPEX.13.006296.
Willner, M., Bech, M., Herzen, J., et al., 2013. Quantitative X-ray phase-contrast computed tomography at 82 keV. Opt. Express 21, 4155–4166.
World Health Organization, 2011. The top 10 causes of death. Available at:, http://www.who.int/mediacentre/factsheets/fs310/en/ (Accessed: 18th July, 2014).
Yaroshenko, A., Meinel, F.G., Bech, M., et al., 2013. Pulmonary emphysema diagnosis with a preclinical small-animal x-ray dark-field scatter-contrast scanner. Radiology 269, 427–433.
Yashiro, W., Terui, Y., Kawabata, K., Momose, A., 2010. On the origin of visibility contrast in x-ray Talbot interferometry. Opt. Express 18, 16890. http://dx.doi.org/10.1364/OE.18.016890.
Zanette, I., Bech, M., Pfeiffer, F., et al., 2011. Interlaced phase stepping in phase-contrast x-ray tomography. Appl. Phys. Lett. 98, 094101.
Zanette, I., Bech, M., Rack, A., et al., 2012. Trimodal low-dose X-ray tomography. Proc. Natl. Acad. Sci. U. S. A. 109, 10199–10204.
Zvezdin, B., Milutinov, S., Kojicic, M., et al., 2009. A postmortem analysis of major causes of early death in patients hospitalized with COPD exacerbation. Chest 136, 376–380.